# Design and Computational Optimization of Elliptical Vibration-assisted Cutting System with a Novel Flexure Structure

Jinguo Han, Jieqiong Lin, Zhanguo Li, Mingming Lu, Jianguo Zhang

***Abstract*—This paper reports on mechanical design, optimization, and experimental testing of a novel piezo-actuated elliptical vibration-assisted cutting (EVC) system constructed by flexure hinges. The stroke and natural frequency were analyzed based on the theoretical modeling. An enhanced central composite design was chosen as the design of experiments methodology to reduce the modeling error, and a non-dominated sorted genetic algorithm-Ⅱ was adopted for structure optimization. The optimized EVC generator was manufactured and experimentally tested to investigate practical properties of the proposed EVC system. It shows that the stroke of input end can reach to 30 μm with a motion resolution of 10 nm, and the first natural frequency can reach to 2600 Hz without considering the manufacturing error. Besides, a relatively small cross-axis coupling ratio (within 0.21%) can be effectively obtained. The developed EVC system is advantageous not only to being equipped with machine tools with various configurations, but also to easily achieving arbitrary vibrations in 3-dimensional space through two actuators, which is especially important for the generation of complex structured surfaces. With the present work, it is of great significance to promote industrial application of EVC techniques.**

***Index Terms*—Elliptical vibration cutting, flexure-based compliant mechanism, optimization design, response surface methodology.**

Manuscript received October 1, 2017; revised October 3, 2017, January 10, 2018, and April 1, 2018; accepted April 29, 2018. This work was supported in part by the Ministry of Science and Technology State Key Support Program (2016YFE0105100), Micro-Nano and Ultra-precision Key Laboratory of Jilin Province (20140622008JC), Science and Technology Development Projects of Jilin Province (20180201052GX, 20180101034JC) and the Education Department Scientific Research Planning Project of Jilin Provincial (JJKH20181038KJ).

Jinguo Han, Jieqiong Lin, Zhanguo Li and Mingming Lu are with the School of Mechatronic Engineering, Changchun University of Technology, Changchun 130012, China (e-mail: hankeyee@163.com, linjieqiong@ccut.edu.cn, lizg79@126.com, lumm@ccut.edu.cn). (Corresponding author: Jieqiong Lin and Zhanguo Li.)

Jianguo Zhang is with the Changchun Institute of Optics, Fine Mechanics and Physics, Chinese Academy of Science, Changchun 130033, China and also with the Department of Mechanical Science and Engineering, Nagoya University, Nagoya 464-8603, Japan (e-mail: zhangjg@ciomp.ac.cn).

## I. Introduction

ELLIPTICAL vibration cutting (EVC) as one of the advanced manufacturing technologies has been gradually used in various applications, such as micro-/nano structures fabrication [1]-[3], optical molds manufacturing [4], composite materials machining [5], [6], and so on [7]-[9]. Due to the characteristics of this novel machining process, many advantages including cutting force reduction, tool life increasing and high-quality surface finishing can be achieved. The feasibility of machining difficult-to-cut materials, especially the ferrous metal [7], [10], [11] and brittle materials [12], [13], was experimentally verified. In general, the elliptical vibration locus of tool cutting edge is generated by piezoelectric actuators (PEAs), and degrees-of-freedom (DOF) of the cutting tool are increased as compared with conventional cutting. The manufacturing performances of EVC are strongly dependent on the EVC system. Hence, the development and optimization design of the EVC system is particularly important in promoting practical industrial applications.

In recent years, on the basis of the fact that flexure-based compliant mechanism can achieve an accurate relative motion in micro/nano scale, it has been successfully applied to many fields, such as micro/nano positioning and manipulation [14]-[16], ultra-precision machining and texturing [1], [17], [18], and piezoelectric actuators [19]. This kind of structure has so many advantageous, such as avoiding energy losses caused by friction, unnecessary of lubrication, absence of hysteresis, compactness, easy to be fabricated, capacity of position resolution in micro/nano scale, and so on. It is considered that the flexure structure may be one of the simple adoption for the EVC system manufacture. For ultra-precision machining, several flexure-based EVC generators have been proposed. For example, a resonant 2-dimensional (2D) EVC generator for a vertical lathe, was developed by Guo et al. for the fabrication of dimple patterns [20]. However, the working frequency is restricted to the resonant frequency. On the contrary, the non-resonant EVC system, which serves as an alternative of the resonant EVC, can obtain a continuous working frequency and large vibration amplitude. However, cross-axis coupling is a serious problem generally happened in the flexure-based mechanisms. Zhu et al. developed a 2D EVC generator for a vertical lathe, and it can achieve a relatively large stroke and low coupling ratio due to the two symmetric compound bridge mechanisms and a Z-shaped flexure hinge mechanism [21]. But the working bandwidth is not very high. Although a serial configuration was adopted by Zhou to achieve complete decoupling, the working bandwidth is severely restricted by the increased moving inertia [22]. Lin et al. proposed a 2D EVC generator for horizontal lathe by using two double parallel four-bar linkage mechanisms (DPFLMs) and two right circular flexure hinges (RCFHs) to achieve a compact structure and low axis coupling [17]. However, there are some shortcomings need to be improved, e.g., the lack of machining DOF and dimension parameters optimization.

Compared with 2D EVC, the 3-dimensional (3D) EVC has more DOF and more flexible in various manufacturing applications [18], [23]. However, the mechanical structures in the state-of-the-art 3D EVC generators are very complicated with relatively large dimensional sizes, and it is usually difficult to precisely control the dynamic motions of the 3D EVC system due to the motion axis increasing. Additionally, these already proposed 2D or 3D EVC generators are only designed for a lathe with specific configuration, e.g., the vertical or horizontal lathe, which strongly restricted EVC system to adapt to different machining conditions. Therefore, a novel flexure-based EVC system, which has the characteristics of compact structure, high machining performance, and high commonality for lathes with different configurations, is of great necessary in promoting the EVC technology to the practical industrial applications.

For EVC generator design, it is important to carry out the dimensional optimization to make an optimal balance among the stroke, working bandwidth, axis coupling and stress concentration. In general, for multi-objective optimization, analytical modeling combines with stochastic algorithms, such as Differential Evolution [21], [24], Genetic Algorithm [25] and Particle Swarm Optimization [26], [27] are usually adopted to achieve global optimum. However, the optimization results are strongly dependent on the accuracy of the mathematical models. As known, the effects of changes in design variables can be quantified by design of experiments (DOE) method effectively. In recent years, the method combining DOE and stochastic algorithms attracts much more attention. Response surface methodology, which has the characteristics of easy iteration and high efficiency, can be used to illustrate the relationship between input independent variables and output responses. In addition, finite element analysis (FEA) has been widely used to analyze characteristics of compliant mechanisms due to its efficiency and accurate estimation. Thus, a FEA-based computational optimization is adopted prior to the fabrication of EVC generator.

As discussed above, an EVC generator combining the simple characteristic of a 2D EVC generator and the multiple DOF characteristic of a 3D EVC generator is a promising choice. Motivated by this, a novel flexure-based universal vibration-assisted cutting system is proposed. It could be applied to various machine tools with different configurations, and it also could achieve arbitrary planar vibration in the 3D space. An improved computational optimization method combining a standard response surface and a multi-objective genetic algorithm (MOGA) is developed for the dimension optimization. A prototype was then manufactured and demonstrated through both theoretical analysis and experimental tests.

This paper is organized as follows: the mechanical design is presented in section II. Static and dynamic modeling is given in section III, where the stroke and natural frequency are analyzed. In section IV, an improved computational optimization method combining a standard response surface and the MOGA is adopted for parameter optimization. Then, the optimization results are assessed in section V. In section VI, a prototype of EVC system is fabricated based on the optimal design, FEA and experimental tests are carried out to give a validation. Finally, the conclusion and future work are described in section VII.

## II. Mechanical Design

A novel flexure-based EVC system is proposed, which combines the simple configuration and multiple DOF. It can provide a new choice for ultra-precision machining and texturing. The mechanical structure of the EVC system is schematically shown in Fig. 1. The overall dimensions of the EVC system are 130 mm×120 mm×90 mm. Fig. 1(a) and (b) show the flexible applications of the proposed EVC system in different machine tools with different configurations. For example, when a cutting tool with a rake angle of 0° is used, the tool rake face is parallel to the ground in Fig. 1(a) and this configuration can be applied to the horizontal lathe. In Fig. 1(b), the tool rake face is normal to the ground and this configuration can be applied to the vertical lathe. As shown in Fig. 1(c), the EVC generator is assembled into a circular orbit which is formed by top cover plate and pedestal. The sensor holder is fixed on the EVC generator by screws. It can be seen in Fig. 1(d) that the capacitance sensors and piezoelectric actuators are supported by the sensor holder and fixed or pre-loaded by screws. The torque gauge is an important part in the present design. It should be noted that the rotation axes of the torque gauge and EVC generator are coincident with each other. And the diamond tool tip is located on the rotation axis. Therefore, an arbitrary spatial vibration can be generated by adjusting the angle between EVC generator and ground through torque gauge only using two PEAs. Thus, the proposed EVC system is much simpler and easy to be controlled as compared with the previous researches [18], [23], [28].

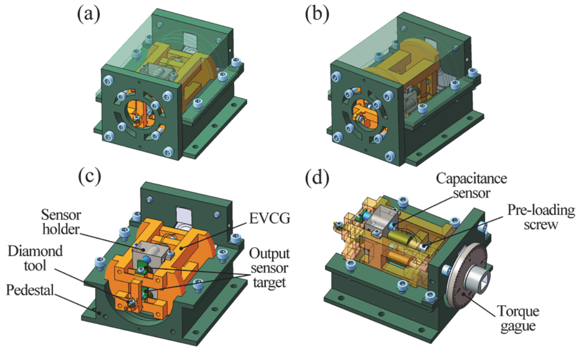


Fig. 1. Mechanical structure of the designed EVC system, (a) configuration for horizontal lathe, (b) configuration for vertical lathe, (c) internal layout, (d) side view.

The mechanical structure design has a significant influence on the application performance of the EVC generator. The structure of the developed EVC generator is shown in Fig. 2(a), two types of compliant mechanism, DPFLM shown in Fig. 2(b) and RCFH based end-effector beam without tool holder shown

This article has been accepted for publication in a future issue of this journal, but has not been fully edited. Content may change prior to final publication. Citation information: DOI 10.1109/TIE.2018.2835425, IEEE Transactions on Industrial Electronics



in Fig. 2(c), are adopted as the motion guidance. Fig. 2(d) and 2(e) show the deformation of upper DPFLM and bottom DPFLM, and Fig. 2(f) shows the deformation of RCFH-based end-effector beam with tool holder. The leaf spring flexure hinge (LSFH) is utilized to constitute the DPFLM. One-way motion and relatively large stroke can easily be obtained because it has mirrored parallel-guiding mechanisms, and this characteristic allows a translational DOF with high off-axis stiffness [29]. In order to avoid the undesired cross coupling, double-symmetric structures or serial configuration are usually used. It is noteworthy that the increasing moving inertia significantly affects the system working bandwidth. In this paper, a parallel configuration is adopted to reduce the crosstalk and RCFH is chosen as the rotation joint due to its precise rotation characteristic. The DPFLM is series connected with the RCFH and this decoupling design is helpful to simplify the control strategy. In addition, there are no lateral motions occur on the basis of the mirror symmetry about the *yz*-plane. The Aluminum 7075-T6 is chosen as the material of EVC generator due to its high stiffness, excellent fatigue strength and light weight. The material properties are concluded as: density ρ=2700 kg/m3, Young's modulus E=70 GPa, Poisson's ratio μ=0.34, and yield strength δs=434 MPa. The other parts of the EVC system are manufactured by steel 45.

## III. Static and Dynamic Modeling

### A. Static Modeling

The DPFLM and RCFH-based end-effector beam play an important role in tertiary motion of the EVC system. Without loss of generality, the deformation is assumed only occur on the flexure hinges. As shown in Fig. 2(d) and (e), the actuation force $F_1$ and $F_2$ are imposed on the midpoint of the upper DPFLM and bottom DPFLM to generate the displacements $\Delta x_1$ and $\Delta x_2$. The deflection angle $\theta_1$ and $\theta_2$ can be obtained on the basis of the equivalent infinitesimal replacement rule as follows:

$$\theta_i \approx \tan\theta_i = \frac{\Delta x_i}{l_1} \qquad (i=1,2) \tag{1}$$

Deformation not only occurs on the parallel compliant LSFH, but also on the rotary RCFHs under the actuation force $F_i$. As shown in Fig. 2(f), the deflection angle of the end-effector beam is defined as $\theta_d$, the rotation angles of the two RCFHs are defined as $\theta_{z1}$ and $\theta_{z2}$, respectively. Because the end-effector beam can be simplified as a rigid bar, and the RCFHs can be simplified as the simple rotate joints, it is appropriate to make an assumption that the rotation angles of RCFHs are equal to the deflection angle of the end-effector beam. Therefore, the deflection angle $\theta_d$ can be derived on the basis of the geometry relationship as follows:

$$\theta_d \approx \tan\theta_d = \frac{|\Delta x_1 - \Delta x_2|}{l} \tag{2}$$

On the basis of the principle of virtual work, the following equation can be derived:

$$\begin{aligned}\frac{1}{2}F_1\Delta x_1+\frac{1}{2}F_2\Delta x_2 &= \frac{1}{2}k_D(\Delta x_1)^2+\frac{1}{2}k_D(\Delta x_2)^2\\ &\quad+\frac{1}{2}k_r(\theta_{z1})^2+\frac{1}{2}k_r(\theta_{z2})^2\end{aligned} \tag{3}$$

According to (2), the (3) can be rewritten as:

$$\begin{aligned}F_1\Delta x_1+F_2\Delta x_2 &= k_D\Delta x_1^{\,2}+k_D\Delta x_2^{\,2}\\ &\quad+2k_r\left(\frac{\Delta x_1-\Delta x_2}{l}\right)^2\end{aligned} \tag{4}$$

According to (4), it is known that no matter which DPFLM actuated, the input stiffness is the same without considering the tool holder due to the symmetry design. Thus, when one DPFLM is actuated, the overall stiffness of the EVC system can be obtained:

$$K_{zi} = k_d + \frac{2k_r}{l^2} \qquad (i=1,2) \tag{5}$$

where $k_d$ denotes the stiffness of the DPFLM, $k_r$ represents the rotary stiffness of the RCFH. The equation of $k_d$ and $k_r$ can be expressed as follows [17], [30]:

$$k_d = \frac{4Eb_1t_1^{\,3}}{l_1^{\,3}} \tag{6}$$

$$k_r = \frac{2Eb_2}{9\pi}\sqrt{\frac{t_2^{\,5}}{r}} \tag{7}$$

where $E$ is Young's modulus, $b_1$ is height of the LSFH, $t_1$ denotes the thickness of LSFH, $l_1$ denotes the length of LSFH, $b_2$ represents the height of RCFH, $t_2$ represents the thickness of RCFH, and $r$ is the radius of RCFH.

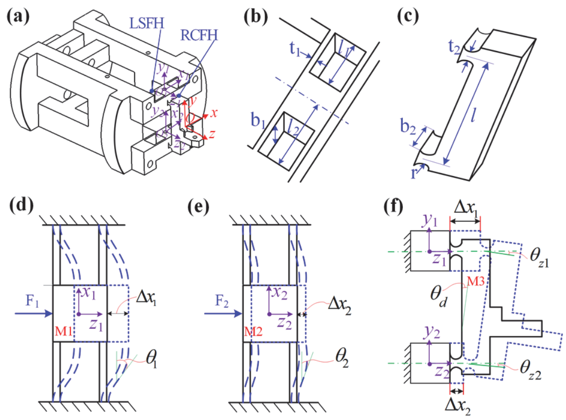


Fig. 2. Schematic of (a) EVC generator, (b) DPFLM, (c) RCFH-based end-effector beam, (d) Upper DPFLM deformation, (e) Bottom DPFLM deformation, and (f) RCFH-based end-effector beam deformation.

It is known that the unload PEA can only output displacement. However, PEA can generate force while it is adopted in a restraint. The output displacement reduction depends on the stiffness of the external mechanical structure. Therefore, the actual displacement of PEA can be expressed as follows:

$$\Delta L = \frac{k_p \Delta L_0 - F_{pre}}{k_p + K_z} \tag{8}$$

where $k_p$ denotes the stiffness of PEA, $F_{pre}$ represents the preloaded force, $\Delta L_0$ is the maximum output displacement of PEA under free expansion, $K_z$ is the input stiffness of the EVC system.

### B. Dynamic Modeling

For the EVC generator, input displacement vector $q = [\Delta x_1, \Delta x_2]^T$ is adopted as the generalized coordinates considering the kinematics relation. It is known that the flexure hinge can be equivalent to a spring [31], thus, the dynamic model of the EVC generator is shown in Fig. 3. Therefore, the kinetic energy of the EVC generator can be obtained:

$$T = \frac{1}{2} M_1 \dot{\Delta x_1}^2 + \frac{1}{2} M_2 \dot{\Delta x_2}^2 + \frac{1}{2} M_3 (\frac{\dot{\Delta x_1} + \dot{\Delta x_2}}{2})^2 + \frac{1}{2} J (\frac{\dot{\Delta x_1} - \dot{\Delta x_2}}{l})^2 \tag{9}$$

where $M_1$ and $M_2$ are the masses of the input end, and $M_3$ is the mass of the end-effector beam, $J$ denotes the rotational inertia of the end-effector beam.

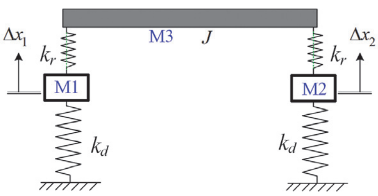


Fig. 3. Dynamic model of the EVC generator.

The potential energy of the EVC generator can be derived as:

$$V = \frac{1}{2} k_d \Delta x_1^2 + \frac{1}{2} k_d \Delta x_2^2 + \frac{1}{2} k_r \theta_{z1}^2 + \frac{1}{2} k_r \theta_{z2}^2 \tag{10}$$

According to the Lagrange's equation, the dynamic model of free vibrations can be deduced without considering the damping effects:

$$\frac{d}{dt}(\frac{\partial T}{\partial \dot{q}}) - \frac{\partial T}{\partial q} + \frac{\partial V}{\partial q} = 0 \tag{11}$$

Substituting (9) and (10) into (11), the dynamic model can be rewritten as follows:

$$\begin{bmatrix} M_1 + \frac{M_3}{4} + \frac{J}{l^2} & \frac{M_3}{4} - \frac{J}{l^2} \\ \frac{M_3}{4} - \frac{J}{l^2} & M_2 + \frac{M_3}{4} + \frac{J}{l^2} \end{bmatrix} \begin{bmatrix} \Delta \ddot{x}_1 \\ \Delta \ddot{x}_2 \end{bmatrix} + \begin{bmatrix} k_d + \frac{2k_r}{l^2} & -\frac{2k_r}{l^2} \\ -\frac{2k_r}{l^2} & k_d + \frac{2k_r}{l^2} \end{bmatrix} \begin{bmatrix} \Delta x_1 \\ \Delta x_2 \end{bmatrix} = 0 \tag{12}$$

On the basis of the linear vibration theory, solving the characteristic equation, the in-plane natural frequency can be deduced as:

$$f_i = \frac{1}{2\pi}\sqrt{\lambda_i} \quad (i = 1, 2) \tag{13}$$

where $\lambda_i$ is the eigenvalues of the characteristic equation.

## IV. Computational Parameter Optimization

### A. Optimization Statement

In order to achieve the application of designed EVC system, two commercially available PEAs were chosen to drive the EVC generator. It has a translational stiffness of 25 N/μm and a maximum free expansion of 42 μm. As an initial design, the parameter values are $t_1 = 1.2mm$, $b_1 = 10mm$, $l_1 = 10mm$, $l_2 = 15mm$, $t_2 = 2mm$, $b_2 = 8mm$, $r = 1.25mm$, and $l = 28mm$, respectively. It is known that the performances of the flexure-based mechanism mainly dependent on the dimension parameters of the flexure hinges. In order to obtain the best performances, the dimensions of the flexure hinges are needed to be further optimization. Considering the compact structure, the design variables which needed to be further optimization are thickness of LSFH $t_1$, thickness of RCFH $t_2$, and radius of RCFH $r$. In order to obtain a safety working condition and high accurate and efficient machining results for different machining objects, the developed EVC generator mechanism is expected to have a relative broad stroke, low working stress, low crosstalk, and high first natural frequency (FNF). Thus, the optimization problem can be stated as follows:

$$\text{Objective:} \quad \begin{cases} \Delta L(t_1, t_2, r) \geq 30\mu m \\ f(t_1, t_2, r) > 3000Hz \end{cases} \tag{14}$$

$$\text{Constraints:} \quad \begin{cases} \frac{\Delta L_c}{\Delta L} < 5\% \\ \sigma_{\max} < \frac{\sigma_s}{n} \end{cases} \tag{15}$$

$$\text{Within ranges:} \quad \begin{cases} 0.5mm \leq t_1 \leq 1.5mm \\ 0.4mm \leq t_{2h} \leq 1.2mm \\ 0.5mm \leq r \leq 1.5mm \end{cases} \tag{16}$$

where $\Delta L$ is the displacement of the actuated input end; $\Delta L_c$ is the crosstalk of the input end without driving signal; $f$ is the first-order natural frequency; $\sigma_s$ denotes the yield strength of the adopted material of EVC generator; $n$ is the safety factor. In this paper, $n$ is selected as higher than 2 considering the working safety. In addition, $t_{2h}$ is half of $t_2$.

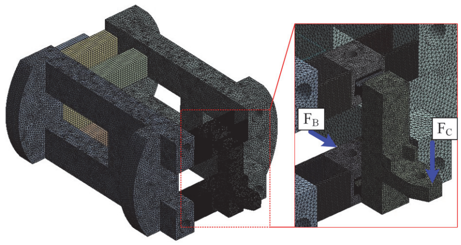


Fig. 4. Meshed model of EVC generator and the load conditions.

This article has been accepted for publication in a future issue of this journal, but has not been fully edited. Content may change prior to final publication. Citation information: DOI 10.1109/TIE.2018.2835425, IEEE Transactions on Industrial Electronics



For the parameter optimization, the external load during the working process is usually ignored [15], [21], [24]-[26]. In this paper, a constant force is applied on the tool holder to simulate the cutting condition in the micromachining process. Taking the mirror symmetry of mechanical structure and the position of tool holder into consideration, the dimension parameters of optimization is only carried out when the bottom DPFLM is actuated due to its relative poor output displacement [17]. As shown in Fig. 4, the meshed model and load conditions for optimization are given. The loads applied to the EVC generator as the actuation force and cutting force were chosen to be ($F_B$, $F_C$) = (100 N, 5 N).

### B. Response Surface Methodology

Considering the modeling error, an enhanced central composite design was chosen as the DOE methodology for a possible better fit for the response surface. In this paper, a standard response surface 2nd-order polynomial was adopted as the meta-model algorithm to make an approximation of the output parameter as a function of the input variables. The modified linear forward stepwise regression was used to select the relevant regression terms and the filtering confidence level is 0.95. In general, a response surface can be described as a quadratic polynomial:

$$y = \beta_0 + \sum_{i=1}^{k} \beta_i x_i + \sum_{i=1}^{k} \sum_{j=i}^{k} \beta_{ij} x_i x_j \tag{17}$$

where $y$ denotes the predicted output parameter, $x$ denotes the design variable, $\beta_0$ denotes the constant terms, $\beta_i$ represents the linear terms, $\beta_{ij}$ represents the quadratic terms, and $k$ represents the number of the design variables.

Usually a second order polynomial just can provide an approximation. In order to improve the quality of the approximation, the Yeo-Johnson transformation model [32] was adopted due to more numerically stable in its back-transformation. As shown in Table I, twenty-nine design points and eight refinement points are used to create the response surface. On the basis of the computational results, the relationship between input variables and output parameters can be easily obtained according to (17). Considering the space limit, the mathematical models will not be given.

The goodness-of-fit can be verified by the coefficient of determination ($R^2$) and adjusted coefficient of determination ($R^2_{adj}$). The value 99.99% of $R^2$ and $R^2_{adj}$ indicate that the response surfaces have a good accuracy. In addition, ten verification points were adopted to demonstrate the effectiveness of the response surfaces as shown in Fig.5. Results show a good effectiveness.

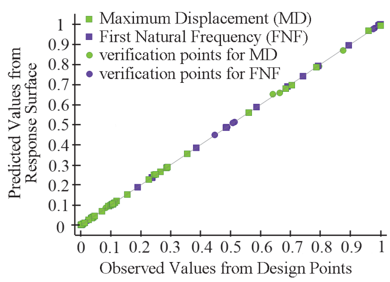


Fig. 5. Comparison between the design points and response surfaces.

### C. Genetic Algorithm

A Non-dominated Sorted Genetic Algorithm-II (NSGA-II), which is based on the controlled elitism concepts, was utilized to perform the optimization process. A fast and non-dominated sorting method was adopted for Pareto ranking. The penalty functions and Lagrange multipliers are not needed because the constraint handling uses the same non-dominance principle as the objectives, which ensures that the unfeasible solutions are always ranked lower than the feasible solutions. The MOGA goes through several iterations retaining the elite percentage of the samples through each iteration allowing the samples to genetically evolve until the best Pareto front has been found. In addition, the Pareto dominance is appropriate especially for the objectives and constraints which are mutually conflicting.

As shown in Fig. 6, the flowchart of the multi-objective optimization procedure, which combines the enhanced central composite design response surface and MOGA optimization algorithm, was given. Therefore, the main process of the optimization can be concluded as follows:

(1) Mechanical design is finished first, static and modal analyses are carried out to obtain the response value for the initial design parameters. (2) A response surfaces methodology is adopted to create a predictive model for the design points and the response values. Then the predicted error should be checked, the other DOE methodology or increase experimental design points should be considered when the error is larger than the requirements. (3) MOGA is adopted to deal with the optimization process via selection, crossover and mutation. The optimization is converged when the maximum allowable Pareto percentage realized. The optimization can be outputted when the predicted error satisfies the requirement, otherwise the design points should be refined to create a new predictive model to continue the optimization process. In this paper, optimal space-filling method is utilized to generate the 100 initial samples. The number of the samples per iteration was also 100. In addition, the maximum allowable Pareto percentage was set to be 90%. The probability of mutation and crossover is, 0.01 and 0.98, respectively.

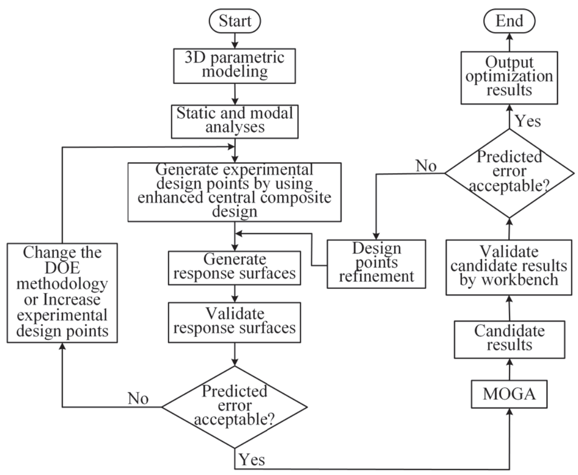


Fig.6. A flowchart of the multi-objective optimization procedure.

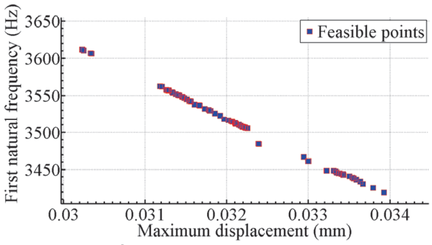


Fig. 7. Pareto optimal front.

TABLE I
DESIGN LAYOUT PLAN AND COMPUTATIONAL RESULTS

| No. | $(t_1, t_{2h}, r)$ | $y_1$ (μm) | $y_2$ (Hz) |
|---|---|---|---|
| 1 | (1, 0.8, 1) | 39.22 | 3024.21 |
| 2 | (0.5, 0.8, 1) | 204.07 | 1205.56 |
| 3 | (0.75, 0.8, 1) | 77.96 | 2088.69 |
| 4 | (1.5, 0.8, 1) | 14.75 | 4949.10 |
| 5 | (1.25, 0.8, 1) | 22.88 | 3985.09 |
| 6 | (1, 0.4, 1) | 42.39 | 3024.68 |
| 7 | (1, 0.6, 1) | 40.94 | 3024.83 |
| 8 | (1, 1.2, 1) | 35.94 | 3020.71 |
| 9 | (1, 1, 1) | 37.50 | 3022.66 |
| 10 | (1, 0.8, 0.5) | 38.66 | 3024.89 |
| 11 | (1, 0.8, 0.75) | 38.97 | 3024.67 |
| 12 | (1, 0.8, 1.5) | 39.60 | 3021.46 |
| 13 | (1, 0.8, 1.25) | 39.42 | 3023.15 |
| 14 | (0.5, 0.4, 0.5) | 245.75 | 1206.41 |
| 15 | (0.75, 0.6 0.75) | 82.67 | 2089.87 |
| 16 | (1.5, 0.4, 0.5) | 15.29 | 4936.04 |
| 17 | (1.25, 0.6, 0.75) | 23.49 | 3983.73 |
| 18 | (0.5, 1.2, 0.5) | 179.06 | 1204.74 |
| 19 | (0.75, 1, 0.75) | 72.64 | 2088.07 |
| 20 | (1.5, 1.2, 0.5) | 13.88 | 4958.22 |
| 21 | (1.25, 1, 0.75) | 22.03 | 3986.64 |
| 22 | (0.5, 0.4, 1.5) | 255.45 | 1208.00 |
| 23 | (0.75, 0.6, 1.25) | 83.85 | 2089.96 |
| 24 | (1.5, 0.4, 1.5) | 15.34 | 4944.24 |
| 25 | (1.25, 0.6, 1.25) | 23.62 | 3984.84 |
| 26 | (0.5, 1.2, 1.5) | 183.93 | 1199.39 |
| 27 | (0.75, 1, 1.25) | 73.90 | 2085.16 |
| 28 | (1.5, 1.2, 1.5) | 14.12 | 4942.53 |
| 29 | (1.25, 1, 1.25) | 22.24 | 3982.35 |
| 30 | (0.6, 0.5, 0.6) | 149.21 | 1547.02 |
| 31 | (0.7, 0.55, 0.7) | 99.64 | 1907.49 |
| 32 | (0.8, 0.7, 0.8) | 68.65 | 2272.73 |
| 33 | (0.9, 0.75, 0.9) | 51.05 | 2646.78 |
| 34 | (1.1, 0.9, 1.1) | 30.64 | 3404.03 |
| 35 | (1.2, 0.95, 1.2) | 24.72 | 3788.50 |
| 36 | (1.3, 1.1, 1.3) | 19.95 | 4175.94 |
| 37 | (1.4, 1.15, 1.4) | 16.68 | 4559.97 |

TABLE II
COMPARISONS OF THREE CANDIDATE POINTS

| Design variables | $t_1$ (mm) | $t_{2h}$ (mm) | $r$ (mm) | $y_1$ (mm) | $y_2$ (Hz) |
|---|---|---|---|---|---|
| Candidate 1 | 1.1535 | 0.40991 | 1.4317 | 0.030233 | 3611.8 |
| Validate1 | / | / | / | 0.029565 | 3612.7 |
| Predicted Error (%) | / | / | / | 2.26 | -0.03 |
| Candidate 2 | 1.1522 | 0.41131 | 1.4765 | 0.030332 | 3607 |
| Validate2 | / | / | / | 0.029644 | 3608.2 |
| Predicted Error (%) | / | / | / | 2.32 | -0.03 |
| Candidate 3 | 1.1392 | 0.40279 | 1.4924 | 0.031288 | 3557.1 |
| Validate3 | / | / | / | 0.030525 | 3557.6 |
| Predicted Error (%) | / | / | / | 2.5 | -0.01 |

TABLE III
COMPARISON BETWEEN INITIAL DESIGN AND OPTIMAL DESIGN

| Output parameters | Initial design | Optimal design | Increment rate (%) |
|---|---|---|---|
| Maximum displacement | 24.514 μm | 29.796 μm | 21.55 |
| First natural frequency | 3788.5 Hz | 3599.5 Hz | -4.99 |
| Axis coupling ratio | 9.93% | 4.25% | -57.2 |
| Maximum stress | 138.73 MPa | 165.87 MPa | 19.56 |

## V. ASSEMENTS OF THE OPTIMAL DESIGN

According to the multi-objective optimization procedure, a series of optimal solutions can be obtained for the Pareto optimal front. As shown in Fig. 7, the maximum displacement and the FNF are mutually conflicting. Moreover, three candidate points and the corresponding results are shown in Table II. It shows that the predicted model has a high accuracy with the predicted error within 3%. Therefore, candidate 1 was chosen as the initial optimal design points considering the highest FNF and relatively high displacement. In addition, the dimension of design variables ($t_1, t_2, r$) are set to be (1.15 mm, 0.82 mm, 1.43 mm) as the best choice considering the manufacturing condition of the prototype. Table III shows the output results as comparing the initial design with the optimal design. It shows that the maximum displacement is increased 21.55% and the rate of the axis coupling ratio is decreased 57.2% as compared with the initial design. Although the FNF has a 4.99% decline, it is high enough for precision micromachining. Additionally, even though the maximum stress has a 19.56% increment, it still smaller than the material allowable stress. Therefore, it could conclude that the optimal design is helpful to improve the comprehensive performance of EVC system.

## VI. PERFORMANCE VALIDATION AND DISCUSSION

### A. Experiment Setup

A prototype of the EVC generator has been manufactured by wire electrical discharge machining to reduce the residual stress and contour errors. The experimental setup is schematically shown in Fig. 8. A power amplifier (E-500, PI Inc.) was utilized to amplify the control signal generated from the Power PMAC

(Delta Tau Inc.) to drive the PEAs (40VS12, Harbin core tomorrow science & technology Co. Ltd). The displacement of the sensor target was gathered by the capacitance transducer and feedback to the controller to form a closed-loop. In addition, a proportion integration differentiation control methodology was adopted to control the EVC system.

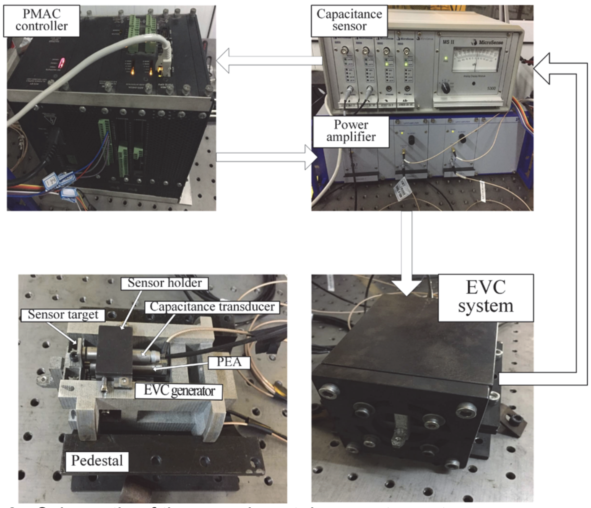


Fig. 8. Schematic of the experimental apparatus setup.

### B. Motion Stroke Analysis, Step Responses and Resolution Tests

According to the kinematical analysis [17], it is reported that the output displacement is almost proportional to the input displacement. In order to investigate the motion stroke, it is necessary to study the maximum displacement of the input end. As shown in Fig. 9, the consecutive step input was applied to the upper and bottom DPFLMs. It can be observed that the output displacement of the DPFLMs along z1 and z2 axes can reach the maximum value, i.e., 37 μm and 31 μm at the maximum input commands. The different outputs may be caused by the asymmetry shape of the tool holder. Moreover, Fig. 9(a) shows that the compliant mechanism cannot track the maximum input command immediately, which demonstrates the tested compliant mechanism is working in the maximum limitation of displacement output. The maximum displacement of the input end can also be determined theoretically by (8) on the basis of the optimal dimension parameters with value of 35 μm, which agrees well with the experiment results. The large input displacement indicates a large output displacement, which is very important for the flexibility of micromachining and microstructure processing in different scales.

On the other hand, in order to investigate the fast response ability of the compliant mechanism, the single step response tests were also carried out. With the same maximum input commands in Fig. 9, Fig. 10 shows that the present compliant mechanism can reach a fast response of 34 μm and 30 μm along $z1$ and $z2$ axes. The measured output displacement has a maximum difference of about 5 μm from the input command value. As the input values exceed the tolerable input regime, the position error is huge. As compared with the maximum output distance in Fig. 9 and Fig. 10, a little deviation is observed although the same maximum input value is adopted. This deviation may be caused by the huge heat generation process when the designed mechanism is working at the limit displacement output conditions. It also shows that the rise time is 4.4 ms and 4.2 ms for upper DPFLM and bottom DPFLM, respectively. In addition, the setting time of two DPFLMs were, respectively, 6.7 ms and 9.06 ms, no steady errors and overshoots were observed. Based on the fundamental findings in Fig. 9 and Fig. 10, the input displacement should be smaller than 34 μm for upper DPFLM and 30 μm for bottom DPFLM during the actual machining process.

In order to investigate the nano-positioning performance of the designed EVC generator, the resolution tests were carried out by applying stair excitation signal to each axis. The duration of one step is set to be 0.4 s. In general, the flexure-based mechanism has a reduced resolution due to the effects of environmental disturbance and quantization error of the D/A converter. The measured results along each axis are illustrated in Fig. 11. From the responses shown in Fig. 11(a) and (b), the resolution along $z1$ and $z2$ axes are approximately 9 nm and 10 nm, respectively, which is very helpful for the precision micro/nano manufacturing.

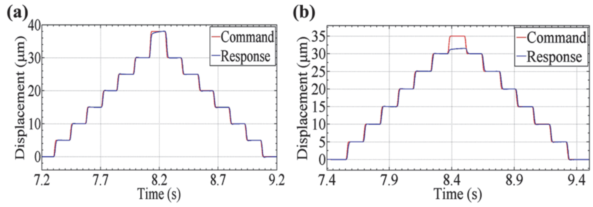


Fig. 9. Motion response for a consecutive step input.

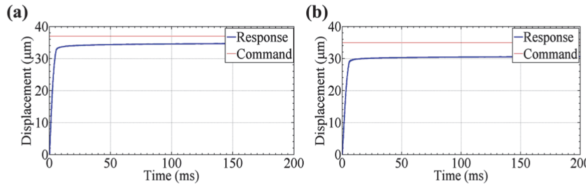


Fig. 10. Step response of (a) upper DPFLM, (b) bottom DPFLM.

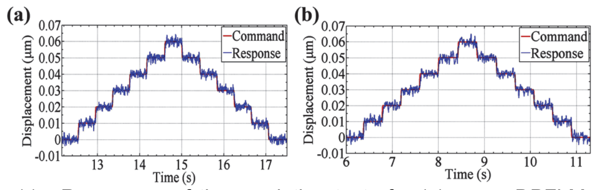


Fig. 11. Responses of the resolution tests for (a) upper DPFLM, (b) bottom DPFLM.

### C. Dynamic Characteristic Analysis and Tests

In order to investigate the dynamic properties of the designed EVC generator, the FEA and swept excitation method are adopted. As shown in Fig. 12, the first four modes of EVC generator without PEAs were extracted by ANSYS software. It can be observed that the first two modes with values of 3599.5 Hz and 3900.2 Hz are coincident with the movement along z axis and pitch, which are the working directions of EVC generator. The values of third and fourth modes are 6561.4 Hz and 6684.9 Hz, respectively, which are coincident with the yaw and the movement along $x$ axis. According to (9)-(13), the theoretical values of first two natural frequencies are 4077.9 Hz and 4384.9 Hz. Setting the results of FEA as the benchmark, the

This article has been accepted for publication in a future issue of this journal, but has not been fully edited. Content may change prior to final publication. Citation information: DOI 10.1109/TIE.2018.2835425, IEEE Transactions on Industrial Electronics



relative deviations between FEA and analytical model are 13.2% and 12.4%, respectively. The acceptable deviations show the feasibility of the analytical model.

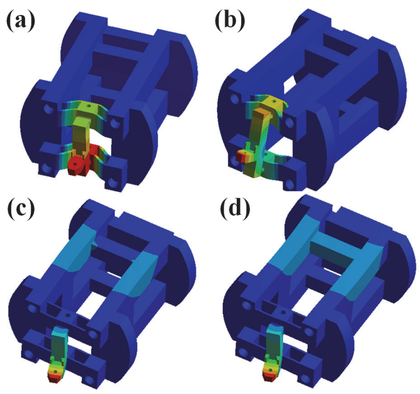


Fig. 12. First four modes of EVC generator, (a) first mode at 3599.5 Hz, (b) second mode at 3900.2 Hz, (c) third mode at 6561.4 Hz, and (d) fourth mode at 6684.9 Hz.

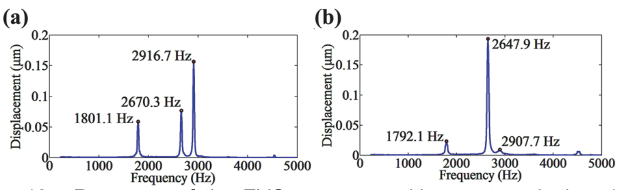


Fig. 13. Response of the EVC generator with swept excitation, (a) response along z1 axis, (b) response along z2 axis.

Swept excitation method was used to investigate the dynamic characteristic of EVC generator due to it is a convenient and expedient method for use. A 3.6 V command signal with varying frequency was chosen and applied to the PEA for each axis. The measured results along $z1$ and $z2$ axes are shown in Fig. 13(a) and (b). It can be obtained from Fig. 13(a) that the first three natural frequencies are 1801.1Hz, 2670.3 Hz, and 2916.7 Hz, respectively. Fig. 13(b) shows the first three natural frequencies are 1792.1 Hz, 2647.9 Hz and 2907.7 Hz, which are coincident with the first three natural frequencies measured along $z1$ axis well due to the symmetrical structure design without considering tool holder. It should be noted that the FNF in experiment is much less than the results of FEA and analytical model. This may be caused by the circular orbit manufacturing error, which leaves gaps between EVC generator and circular orbit. After assembly, the part of the EVC generator, which is away from the DPFLM, has space for movement along $y$ axis. However, the trends of the second and the third natural frequencies of experiment agree well with the first two modes of FEA and analytical model. The frequencies obtained by experiment are relatively smaller due to: (1) a higher increase in the equivalent masses compared with the increase in stiffness; (2) manufacturing errors of the EVC system; (3) lower Young's modulus of the materials; (4) imperfect contacts between PEA and input ends, etc.

### *D. Tracking Accuracy and Cross-Axis Coupling*

In this paper, decoupling was achieved through structure design. The results of tracking error and coupling error were obtained by actuating the PEA only in one axis, while the other axis has no input signal. As shown in Fig. 14(a), when the PEA which is along the $z1$ axis was actuated only, the maximum tracking error of upper DPFLM is 0.7 μm, which is 2.9% of the maximum input displacement. The maximum parasitic motion of $z2$ axis is 0.05 μm, which is 0.21% of the maximum input displacement of $z1$ axis. Similarly, the results shown in Fig. 14(b) indicate that the maximum tracking error of bottom DPFLM is 0.72 μm, which is 3% of the maximum input displacement, and the maximum parasitic motion of $z1$ axis is within 0.035 μm, which is about 0.15% of the maximum input displacement. Therefore, it can be concluded that the tracking accuracy of EVC generator is excellent and the decoupling design is much effective.

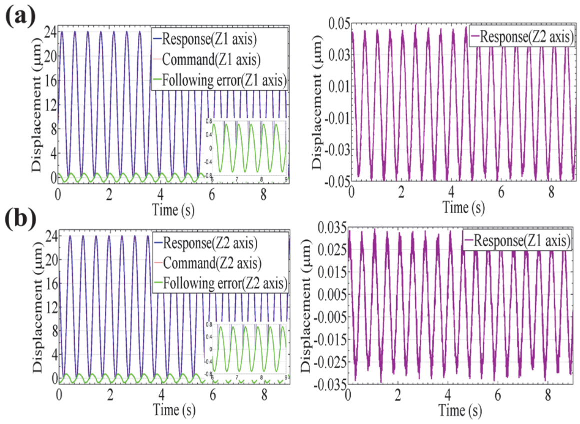


Fig. 14. Results of sinusoidal motion tracking, and parasitic motion for (a) z1 axis and z2 axis, (b) z2 axis and z1 axis.

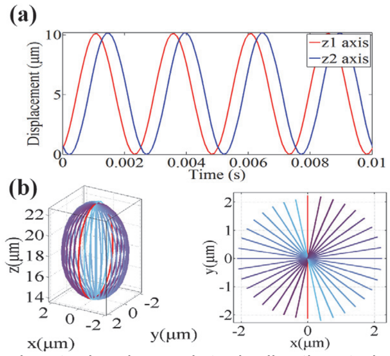


Fig. 15. The input signals, and tool vibration trajectory, (a) the displacement signal at input ends, (b) the synthetic spatial elliptical trajectory and its projection in xy plane.

### *E. Analysis of Elliptical Trajectory Generation*

The objective of this paper is to develop a novel universal vibration-assisted cutting system for various machine tools with different configuration. It can generate arbitrary elliptical vibration in 3D space due to the deliberately designed structure. In order to investigate the trajectory of the tool tip, two input signals with amplitude of 5 μm and frequency of 400 Hz are adopted as shown in Fig. 15(a). According to the kinematic relationship between input end and output end, the tool tip trajectory is shown in Fig. 15(b). In Fig. 15(b), the red ellipse is located in the $yz$ plane, the others with different colors are the elliptical vibration trajectory in 3D space. It shows that the arbitrary space elliptical vibration can be obtained easily by adjusting the angle between EVC generator and ground through torque gauge only using two PEAs.

This article has been accepted for publication in a future issue of this journal, but has not been fully edited. Content may change prior to final publication. Citation information: DOI 10.1109/TIE.2018.2835425, IEEE Transactions on Industrial Electronics



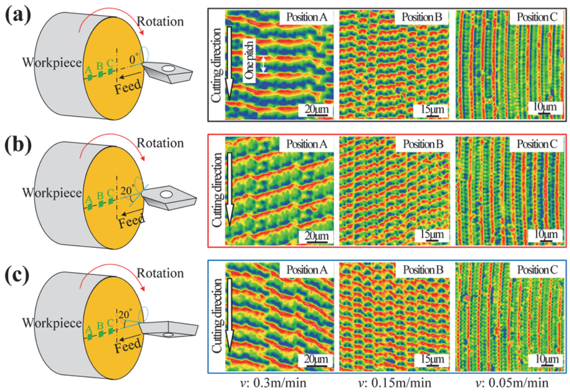


Fig. 16. Surface profile of three different cutting configurations.

### *F. Performance tests on the machine*

In order to verify the feasibility of the proposed cutting system, the face turning processes were experimentally carried out. 6061Al with a diameter of 12.7 mm is adopted as the workpiece material. A polycrystalline diamond (PCD) tool, with a nose radius of 0.4 mm, a rake angle of 0 deg and a clearance angle of 10 deg, is used. The amplitudes of elliptical vibration are set to be 5.6 $\mu m_{0\text{-}p}$ and 3.5 $\mu m_{0\text{-}p}$ at 200 Hz, respectively, and a phase difference is about 70 deg. The workpiece is attached to the spindle with a rotation speed of 15 rpm. A depth of cut of 10μm and a feed rate of 200 μm/min are adopted. The machined surface quality is experimentally investigated with different vibration planes in 3D space. The surface topography was measured by an optical surface profiler (ZygoNewview, USA).

Figure 16 shows the machined surfaces with different vibration planes and nominal cutting speed from 0.05 m/min to 0.3 m/min. With a relatively large cutting speed of 0.3 m/min, the cutting process becomes elliptical vibration texturing [20]. A part of elliptical vibration trajectory is superimposed on the machined surface in each vibration, resulting in regular undulation on the finished surface. The textured structure has a stable pitch value of 20 μm along the cutting direction and a structural height of about 1.8 μm. With decreasing the cutting speed into 0.05 m/min, the vibration mark with a pitch value of 4 μm and structural height of about 0.2 μm is generated on the machined mirror surface. The stability and feasibility of the proposed vibration cutting system is experimentally verified. It should be noted that the material grain boundary also has an influence on the present machined surface roughness. Furthermore, the residual microstructure generated at different positions and postures may have potential applications in hybrid micro-optics, surface wettability modifications and tribological control.

## VII. Conclusion

A flexure-based universal vibration-assisted cutting system has been proposed and tested in this paper. In this system, an EVC generator actuated by PEAs was designed and optimized by an improved algorithm which combining a standard response surface and the MOGA. The static modeling and dynamic modeling were carried out to investigate the stroke response and the bandwidth. As compared with the analyzed results obtained from FEA and theoretical model, the trend of experimental results agrees well with them. Experimental tests show that the performances of upper DPFLM are better than that of bottom DPFLM due to the non-symmetrical design of the tool holder. The stroke of input end of EVC generator can reach to 30 μm with a motion resolution of 10 nm. The FNF can reach to 2600 Hz without considering the effect of manufacturing error, which enables the EVC system has a high working bandwidth. In addition, the tracking accuracy and axis coupling ratio are respectively within 3% and 0.21% indicating an excellent ability of tracking and decoupling. The feasibility of the developed vibrator is experimentally verified. In future work, the machining experiments are required in detail to study the micromachining performance of the developed EVC system.

## References

[1] Z. Zhu, S. To, S. Zhang, and X. Zhou, "High-throughput generation of hierarchical micro/nanostructures by spatial vibration-assisted diamond cutting," *Adv. Mater. Interfaces.*, vol. 3, no. 4, pp. 1500477, Feb. 2016.

[2] J. Zhang, N. Suzuki, Y. Wang, and E. Shamoto, "Ultra-precision nano-structure fabrication by amplitude control sculpturing method in elliptical vibration cutting," *Precis. Eng.*, vol. 39, pp. 86-99, Jul. 2015.

[3] Y. Yang, Y. Y. Pan, and P. Guo, "Structural coloration of metallic surfaces with micro/nano-structures induced by elliptical vibration texturing," *Appl. Surf. Sci.*, vol. 402, pp. 400-409, Apr. 2017.

[4] N. Suzuki, M. Haritani, J. Yang, R. Hino, and E. Shamoto, "Elliptical vibration cutting of tungsten alloy molds for optical glass parts," *Cirp Ann-Manuf Techn.*, vol. *56,* no. 1, pp.127-130, May. 2007.

[5] W. Xu, L. Zhang, and Y. Wu, "Elliptic vibration-assisted cutting of fibre-reinforced polymer composites: understanding the material removal mechanisms," *Compos. Sci. Technol.*, vol. 92, pp. 103–111, Feb. 2014.

[6] J. Liu, D. Zhang, L. Qin, and L. Yan, "Feasibility study of the rotary ultrasonic elliptical machining of carbon fiber reinforced plastics (CFRP)," *Int. J. Mach. Tool. Manu.*, vol. 53, no. 1, pp. 141–150, Feb. 2012.

[7] H. Saito, H. J, and E. Shamoto, "Elliptical vibration cutting of hardened die steel with coated carbide tools," *Precis. Eng.*, vol. 45, pp. 44-54, Jul. 2016.

[8] H. Jung, T. Hayasaka, and E. Shamoto, "Mechanism and suppression of frictional chatter in high-efficiency elliptical vibration cutting," *Cirp Ann-Manuf Techn.*, vol. 65, no. 1, pp. 369-372, Apr. 2016.

[9] Y. Lu, P. Guo, P. Pei, and K. F. Ehmann, "Experimental studies of wettability control on cylindrical surfaces by elliptical vibration texturing," *Int. J. Adv. Manuf. Technol.*, vol.76, no. 9-12, pp. 1807-1817, Feb. 2015.

[10] H. Saito, H. Jung, E. Shamoto, T. C. Wu, and J. T. Chien, "Mirror Surface Machining of High-Alloy Steels by Elliptical Vibration Cutting with Single-Crystalline Diamond Tools: Influence of Alloy Elements on Diamond Tool Damage," *Precis. Eng.*, vol. 49, pp. 200-210, Jul. 2017.

[11] E. Shamoto, and T. Moriwaki, "Ultaprecision diamond cutting of hardened steel by applying elliptical vibration cutting," *Cirp Ann-Manuf Techn.*, vol. 48, no. 1, pp. 441-444, 1999.

[12] Z. Zhu, S. To, G. Xiao, K. F. Ehmann, and G. Zhang," Rotary spatial vibration-assisted diamond cutting of brittle materials," *Precis. Eng.*, vol. 44, pp. 211-219, Apr. 2016.

[13] Z. Liang, X. Wang, Y. Wu, L. Xie, L. Jiao, and W. Zhao," Experimental study on brittle–ductile transition in elliptical ultrasonic assisted grinding (EUAG) of monocrystal sapphire using single diamond abrasive grain," *Int. J. Adv. Manuf. Technol.*, vol. 71, pp. 41-51, Aug. 2013.

[14] Y. Li, and Q. Xu, "A novel piezoactuated XY stage with parallel, decoupled, and stacked flexure structure for micro-/nanopositioning," *IEEE Trans. Ind. Electron.*, vol.58, no.8, pp. 3601-3615, Aug. 2011.

[15] Y. Qin, B. Shirinzadeh, Y. Tian, D. Zhang, and U. Bhagat, "Design and computational optimization of a decoupled 2-DOF monolithic mechanism," *IEEE-ASME T. Mech.*, vol.19, no. 3, pp. 872-881, Jun. 2014.

[16] D. Wang, Q. Yang, and H. Dong, "A monolithic compliant piezoelectric-driven microgripper: Design, modeling, and testing," *IEEE-ASME T. Mech.*, vol.18, no. 1, pp. 138-147, Feb. 2013.

[17] J. Lin, J. Han, M. Lu, B. Yu, and Y. Gu, "Design, analysis and testing of a new piezoelectric tool actuator for elliptical vibration turning," *Smart Mater. Struct.,* vol. 26, no. 8,Jul. 2017.

[18] Z. Zhu, S. To, K. F. Ehmann, and X. Zhou, "Design, analysis, and realization of a novel piezoelectrically actuated rotary spatial vibration system for micro-/nano-machining," *IEEE-ASME T. Mech.,* vol. 22, no. 3, pp. 1227-1237, Jun. 2017.

[19] T. Cheng, M. He, H. Li, X. Lu, and H. Zhao, "A Novel Trapezoid-Type Stick-Slip Piezoelectric Linear Actuator Using Right Circular Flexure Hinge Mechanism," *IEEE Trans. Ind. Electro.,* vol. 64, no. 7, pp. 5545-5552, Jul. 2017.

[20] P. Guo, and K. F. Ehmann, "Development of a tertiary motion generator for elliptical vibration texturing," *Precis. Eng.,* vol. 37, no. 2, pp. 364-371, Apr. 2013.

[21] W. L. Zhu, Z. Zhu, Y. He, and K. F. Ehmann, "Development of a Novel 2D Vibration-assisted Compliant Cutting System for Surface Texturing," *IEEE-ASME T. Mech.*, vol. 22, no. 4, pp. 1796-1806, Aug. 2017.

[22] X. Zhou, C. Zuo, Q. Liu, R. Wang, and J. Lin, "Development of a double-frequency elliptical vibration cutting apparatus for freeform surface diamond machining," *Int. J. Adv. Manuf. Technol.,* vol. 87, no. 5-8, pp. 2099-2111, Mar. 2016.

[23] T. Wada, M. Takahashi, T. Moriwaki, and K. Nakamoto, "Development of a three axis controlled fast tool servo for ultra precision machining (1st report)-development of 3-axis FTS unit and evaluation of its characteristics," *J. Jpn. Soc. Precis. Eng.,* vol. 73, no. 12, pp. 1345–1349, 2007.

[24] Z. Zhu, X. Zhou, Q. Liu, and S. Zhao, "Multi-objective optimum design of fast tool servo based on improved differential evolution algorithm," *J. Mech. Sci. Technol.*, vol. 25, no. 12, pp. 3141-3149, Dec. 2011.

[25] S. Xiao and Y. Li, "Optimal design, fabrication, and control of an XY micropositioning stage driven by electromagnetic actuators," *IEEE Trans. Ind. Electro.,* vol. 60, no. 10, pp. 4613-4626, Oct. 2013.

[26] Y. Li and Q. Xu, "A totally decoupled piezo-driven xyz flexure parallel micropositioning stage for micro/nanomanipulation," *IEEE T. Autom. Sci. Eng.*, vol. 8, no. 2, pp. 265–279, 2011.

[27] R. Wang and X. Zhang, "Parameters optimization and experiment of a planar parallel 3-dof nanopositioning system," *IEEE Trans. Ind. Electro.*, vol. 65, no. 3, pp. 2388-2397, Mar. 2018.

[28] J. Lin, M. Lu, and X. Zhou, "Development of a Non-Resonant 3D Elliptical Vibration Cutting Apparatus for Diamond Turning," *Exp. Techniques.*, vol. 2016, no. 40, pp. 173-183, Jul. 2013.

[29] L. L. Howell, C. M. Dibiasio, M. A. Cullinan, R. M. Panas, and M. L. Culpepper, "A pseudo-rigid-body model for large deflections of fixed-clamped carbon nanotubes," *J. Mech. Robot.,* vol. 2, no. 3, pp. 034501. Jul. 2010.

[30] J. M. Paros, and L. Weisbord, "How to design flexure hinges," *Mach. Des.,* vol. 37, pp. 151-156, Nov. 1965.

[31] H. H. Pham, and I. M. Chen, "Stiffness modeling of flexure parallel mechanism," *Precis. Eng.,* vol. 29, no. 4, pp. 467-478, Oct. 2005.

[32] I. K. Yeo, and R. A. Johnson, "A new family of power transformations to improve normality or symmetry," *Biometrika.*, vol. 87, no. 4, pp. 954-959, Dec. 2000.


**Jinguo Han** was born in Shandong province, China, in 1989. He received the M.S. degree from Changchun University of Technology, Changchun, China, in 2015. He is currently pursuing the Ph.D. degree in the School of Mechatronic Engineering, Changchun University of Technology. His research interests include ultraprecision machining of complex surfaces and micro/nano structures, design of mechatronic systems for ultra-precision manufacturing.

**Jieqiong Lin** received the Ph.D. degree in mechanical manufacturing from the Jilin University of Technology, Changchun, China, in 2005. She is currently a Professor with the School of Mechatronic Engineering, Changchun University of Technology. She is an active researcher who focuses on ultra-precision machining of complex surfaces and difficult-to-cut materials, large area laser processing, precision polishing, micro/nano-positioning of cutting tool, modeling and control of ultra-precision cutting.

**Zhanguo Li** received the Ph.D. degree from the Beijing Institute of Technology, Beijing, China, in 2004. He is currently a Professor with the School of Mechatronic Engineering, Changchun University of Technology. His research interests are focused on digital design of precision machinery, dynamic design and performance evaluation of automobile belt drive and ultra-precision machining technology.

**Mingming Lu** received the Ph.D. degree in mechanical manufacturing from the Jilin University of Technology, Changchun, China, in 2014. He is currently a Lecturer with the School of Mechatronic Engineering, Changchun University of Technology. His research interests are focused on three-dimensional elliptical vibration-assisted cutting, Vibration assisted swing cutting, micro/nano-positioning of cutting tool, modeling and control of ultra-precision cutting.

**Jianguo Zhang** received his B.S. and M.S. degrees in mechanical engineering from Harbin Institute of Technology, China, in 2008 and 2010, respectively; and Ph.D. degree in the department of mechanical science and engineering from Nagoya University, Japan, in 2014. After a brief experience as an assistant researcher in Changchun Institute of Optics, Fine Mechanics and Physics in China, he joined Nagoya University as a designated assistant professor at the Department of Aerospace Engineering in 2017. His research interests include the elliptical vibration cutting technology and the precise fabrication of functional micro/nano structures on difficult-to-cut materials. With the practical research of high-accuracy amplitude control sculpturing method in elliptical vibration cutting, he won the Young Researcher Award in Japan Society for Precision Engineering 2015.